Geophysical Research Letters

RESEARCH LETTER
10.1029/2019GL085446

STEVE and the Picket Fence: Evidence of Feedback-Unstable Magnetosphere-Ionosphere Interaction

Evgeny Mishin[1] and Anatoly Streltsov[2,3]

[1]Space Vehicles Directorate, Air Force Research Laboratory, Kirtland AFB, Albuquerque, NM, USA, [2]Department of Physical Sciences, Embry-Riddle Aeronautical University, Daytona Beach, FL, USA, [3]Summer Faculty, AFRL/Space Vehicle Directorate, Albuquerque, NM, USA

Key Points:
- Feedback-unstable magnetosphere-ionosphere interaction in the presence of energetic electron precipitation explains the Picket Fence formation
- Thermal excitation of the red-line emission in the low-density SAID channel is inhibited by inelastic collisions with molecular nitrogen
- To understand the STEVE continuum, transitions between vibrationally excited molecular states in the SAID channel should be taken into account

Supporting Information:
- Figure S1

Correspondence to:
E. Mishin,
evgeny.mishin@us.af.mil

Citation:
Mishin, E., & Streltsov, A. (2019). STEVE and the picket fence: Evidence of feedback-unstable magnetosphere-ionosphere interaction. *Geophysical Research Letters*, *46*, 14,247–14,255. https://doi.org/10.1029/2019GL085446

Received 17 SEP 2019
Accepted 9 DEC 2019
Accepted article online 10 DEC 2019
Published online 23 DEC 2019

Abstract This paper aims to extend the understanding of Strong Thermal Emission Velocity Enhancement (STEVE) and the Picket Fence related to strong subauroral ion drifts (SAID). We numerically demonstrated that precipitating energetic electrons are critical for the structuring of the Picket Fence. It is created by feedback-unstable magnetosphere-ionosphere interactions driven by the SAID electric field when the Hall conductance created by energetic (≥1 keV) electrons exceeds the Pedersen conductance. We show that thermal excitation of the red-line emission in STEVE is inhibited by inelastic collisions with molecular nitrogen. Suprathermal (≤500 eV) electrons coming from the turbulent plasmasphere appear to be the major source. We also show that the chemiluminescencent and radiative attachment reactions do not explain the short-wavelength part of the STEVE continuum and argue that accounting for vibrational excitation may resolve the problem. Atmosphere's upwelling due to enhanced ion-neutral drag leads to the increased abundance of molecular components relative to atomic oxygen.

1. Introduction

Skyglow in the form of a narrow in magnetic latitude, east-west-aligned mauve "ribbon" and occasionally green rayed "Picket Fence" equatorward of the auroral zone was often reported by amateur photographers. MacDonald et al. (2018) have named the mauve arcs as Strong Thermal Emission Velocity Enhancement (STEVE) because of the relation to strong plasma streams – subauroral ion drifts (SAID), with highly elevated electron temperature, $T_e \geq 5000$ K. Their features have been detailed by Gallardo-Lacourt, Liang, et al. (2018), Gallardo-Lacourt, Nishimura, et al. (2018), Nishimura et al. (2019), and Archer, Gallardo-Lacourt, et al. (2019). In particular, Gallardo-Lacourt, Nishimura, et al. (2018) statistical study shows that STEVE occurred during the recovery phase of substorms. Nishimura et al. (2019) have found that energetic (~10 keV) electrons detached from the plasma sheet were present in the conjugate region of the Picket Fence-related SAID region and were absent in the STEVE region. Using citizen scientists' data, Archer, St.-Maurice, et al. (2019) have estimated the height extent of STEVE and Picket Fence as 130–270 and 95–150 km, respectively.

Gillies et al. (2019) performed the first spectroscopic observations of the STEVE and Picket Fence emissions supporting Nishimura et al.'s (2019) conclusion that the Picket Fence is, in fact, a rayed subauroral aurora. They found that the STEVE color is determined by an intensified 400–800 nm continuum that dominates the red-line emission. However, the question as to why the "extreme" SAID parameters cause the greatly enhanced continuum and weak red-line emission, as opposed to SAR arcs, remains unanswered. Furthermore, the mechanism of small-scale structuring of the electron precipitation that creates the Picket Fence has not even been discussed so far.

This paper aims to understand the underlying mechanism of the Picket Fence structure and the STEVE color. We demonstrate that the Picket Fence structure can be created by feedback-unstable magnetosphere-ionosphere interactions driven by the SAID electric field in the presence of energetic electrons producing the ionospheric Hall conductance, Σ_H, greater than the Pedersen conductance, Σ_P. Then we show that inelastic electron collisions with molecular nitrogen, N_2, inhibit thermal excitation of the red-line emission in the low-density SAID/STEVE region. Suprathermal electrons coming from the turbulent plasmasphere boundary layer (e.g., Mishin, 2013; Mishin & Sotnikov, 2017) appear to be the major excitation source. We also show that the chemiluminescent and radiative attachment reactions do not explain the

10.1029/2019GL085446

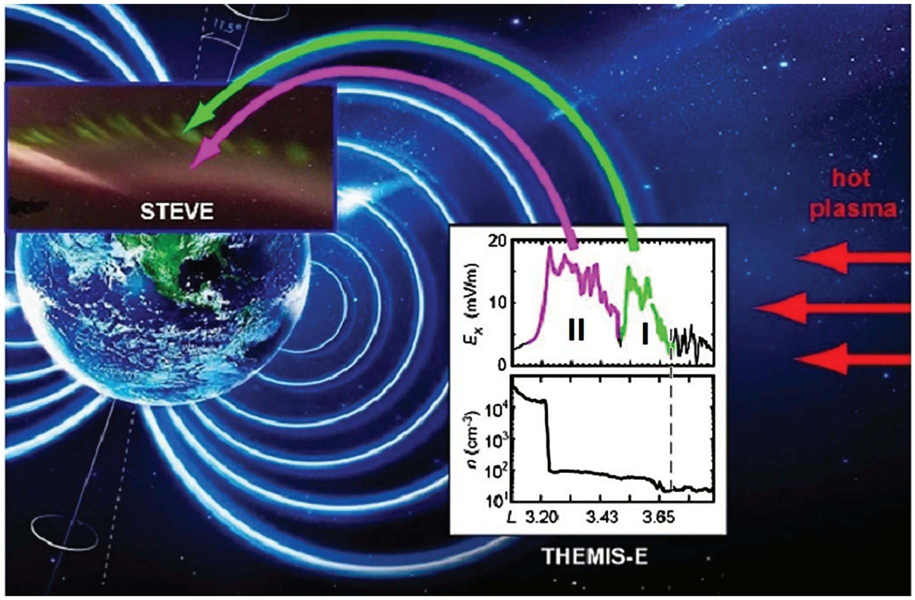

Figure 1. Schematic illustration of the 8 May 2016 STEVE event (Nishimura et al., 2019). Left inset: The green Picket Fence and mauve ribbon in the ionosphere. Right inset: The double SAID electric field, $\mathbf{E}_X$, in mV/m and cold plasma density from THEMIS-E in the subauroral plasmasphere. The outermost SAID (I, green) is coincident with precipitating electrons and maps into the fence, while the innermost SAID (II, magenta) maps into the ribbon. The vertical dashed line indicates the plasma sheet boundary. White curves show the dipole magnetic field. Red arrows indicate earthbound mesoscale (hot) plasma flows.

short-wavelength part of the STEVE continuum and argue that its interpretation requires vibrationally excited molecular states. The increased abundance of molecular species relative to atomic oxygen, O, is due to the atmosphere's upwelling caused by ion drag in strong ion drift channels (e.g., Millward et al., 1993; Aruliah et al., 2005; Mishin et al., 2007).

2. Modeling the Picket Fence Structure

Figure 1 schematically illustrates the 8 May 2016 event (Nishimura et al., 2019, Fig. 1a) consisting of the green Picket Fence poleward of STEVE superimposed on the scaled dipole magnetic field (B_0). It also shows the SAID (outward) electric field, E_X, and plasmaspheric density from the THEMIS-E satellite in the plasmasphere (Nishimura et al., 2019, Fig. 4). The electric field in the outermost SAID-I (green) is coincident with energetic electrons and maps into the Fence, while the SAID-II (magenta) maps into STEVE. The Picket Fence resembles a rayed auroral arc resulting from a small-scale structuring of the precipitating flux along the Hall current direction, $[\mathbf{E}_X \times \mathbf{B}_0]$. We underscore that whenever the concurrent satellite data were available in both hemispheres, the observed SAID events, including particle precipitation, were magnetically conjugate (e.g., Figure S1 in the supporting information; more events can be found in Mishin et al. (2017)).

In order to simulate a rayed auroral arc, Jia and Streltsov (2014) developed a three-dimensional (3-D), two-fluid MHD model of feedback-unstable magnetosphere-ionosphere interactions. This model includes the Pedersen and Hall currents that provide closure of field-aligned currents (FACs) carried by small-scale Alfvén waves generated by the ionospheric feedback instability (IFI) driven by a meridional electric field, E_X. The ionospheric feedback process amplifies small-scale Alfvén waves by virtue of overreflection from the ionosphere, which is caused by the shear convection flow consequent to the altitudinal dependence of ion-neutral collisions (e.g., Trakhtengertz & Feldstein, 1991). In particular, for low E-region plasma densities, $n_{0E} \leq 10^4$ cm^{-3}, the IFI threshold for wavelengths ~1–10 km is approximately $E_{th} \approx 50\omega_{ci}/\nu_{i0}$ mV/m (Trakhtengertz & Feldstein, 1991). Here ω_{ci} is the ion gyrofrequency, and ν_{i0} ($\gg \omega_{ci}$) is the ion-neutral collision frequency at the bottom of the E layer.

As the altitude extent of the conducting bottom of the ionosphere is much less than the parallel wavelength, it is usually approximated by a narrow slab with the uniform density and electric field in order to minimize

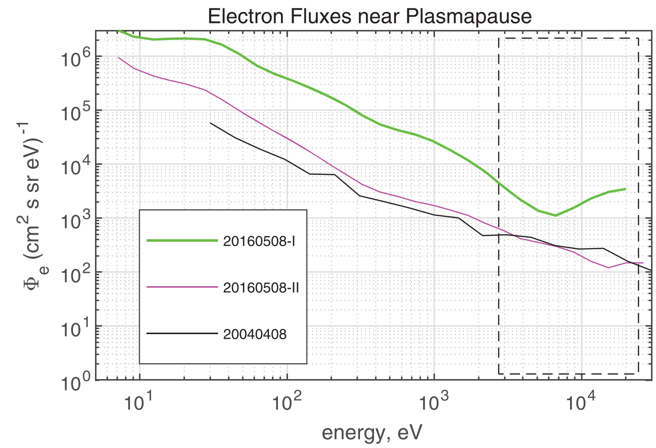

Figure 2. Variation of the electron differential number fluxes with energy. The fluxes from THEMIS-E during the Nishimura et al. (2019) STEVE event on 8 May 2016 (SAID-I, green; SAID-II, magenta) and DMSP F16 (black) during a typical SAID event on 8 April 2004 (Puhl-Quinn et al., 2007) are averaged over the corresponding SAID region. The fluxes inside a rectangle can penetrate below ~120 km and create the Hall conductivity, Σ_H. The THEMIS-E data are provided by Y. Nishimura.

computing time. The magnetospheric part describes dispersive Alfvén waves in an axisymmetric dipole magnetic field using equations for the electron parallel momentum and continuity of the density and current. The ionospheric part is given by a system of equations, which connects the electric field and the plasma density in the ionosphere with the FAC density, $j_{\|}$, and forms a positive feedback loop, $\delta\Sigma(\delta n) \rightarrow \delta j_{\|} \rightarrow \delta n$ (see Streltsov & Mishin (2018a,b) for details).

In a 2-D model, without the Hall current, the Pedersen current, which closes the east-west-aligned sheets of upward and downward FACs, has the form of a strip between the current sheets. Thus, the IFI-generated structures are simply east-west-aligned strips of smaller dimensions determined by the wavelength of the most unstable Alfvén wave (Streltsov & Mishin, 2003; Streltsov & Foster, 2004; Streltsov & Mishin, 2018a, b). With a finite Hall conductance, the total ionospheric current flows under some angle to the direction of the driving field, E_X. That is, the Hall conductivity causes rotation of the IFI-generated ionospheric current and electric field leading to the formation of a chain of vortices within the initial strip. As a result, initially $[E_X \times B_0]$-aligned sheets of FACs turn into a series of small-scale rays or "pickets" along $[E_X \times B_0]$ when Σ_H exceeds Σ_P (Jia & Streltsov, 2014).

We use the particle data measured in the southern hemisphere during the Nishimura et al. (2019) event to specify the ionospheric conductances at the northern magnetic footpoints. Figure 2 shows electron differential number fluxes, $\Phi_e(\epsilon)$, from THEMIS-E inside the SAID-I and II regions (see Figure 1) and, for comparison, from the DMSP F16 satellite SAID event during an individual substorm on 8 April 2004 (Puhl-Quinn et al., 2007). The fluxes are averaged over the corresponding SAID regions. The suprathermal population between ϵ ~30 and 500 eV is a typical feature of SAID resulting from nonlinear wave heating in the turbulent plasmasphere boundary layer (Mishin, 2013; Mishin & Sotnikov, 2017).

The energy range marked by a rectangle in Figure 2 indicates electrons producing ionization below ~120 km where Σ_H becomes significant (e.g., Vallance Jones, 1974; Robinson et al., 1987). The flux in the SAID-I region is significantly greater than the others, particularly in the rectangle. The Σ_H/Σ_P ratio can be found from the well-established Robinson et al. (1987) formula, $\Sigma_H/\Sigma_P \approx 0.45\hat{\epsilon}^{0.85}$, where the mean precipitation energy, $\hat{\epsilon}$, is in keV. Using this formula with $\hat{\epsilon}$ calculated from $\Phi_e(\epsilon)$ in Figure 2, we obtain that only the SAID-I flux makes Σ_H greater than Σ_P (viz., $\Sigma_H \approx 2.2\Sigma_P$) needed to create a rayed structure by the IFI.

We have employed a 3-D MHD model (Jia & Streltsov, 2014) in the SAID-I region (Figure 1) between L-shells 3.2 and 3.4 for max(E_X) =50 mV/m in the ionosphere, taking a 1.0° azimuthal extent of the simulation domain with $\Sigma_H/\Sigma_P = 0$ and 2. Figure 3 shows isocontours of upward (yellow) and downward (blue) FACs at the ionospheric boundary of the simulation domain at the altitude of 110 km in saturation. In agreement with Jia & Streltsov (2014), 2-D current sheets at $\Sigma_H = 0$ become small-scale filaments along $[\mathbf{E}_X \times \mathbf{B}_0]$ at $\Sigma_H/\Sigma_P = 2$. As upward FACs contain precipitating electrons, their structure mimics the optical structure.

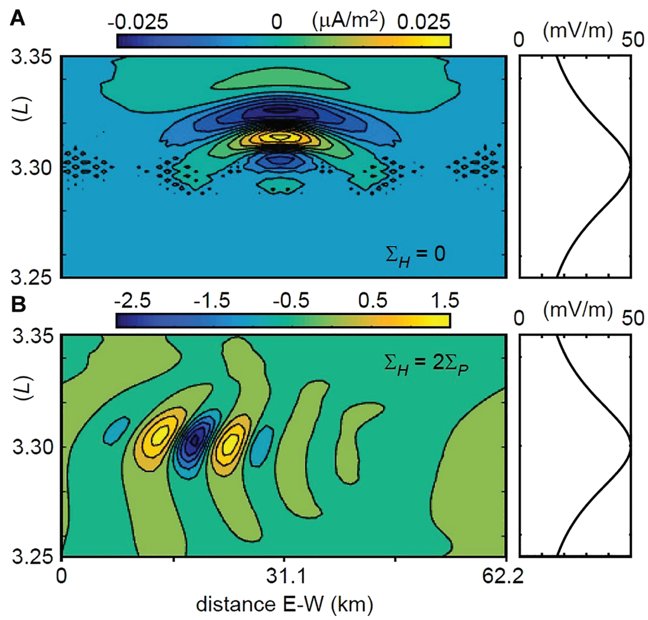

Figure 3. Isocontours of downward (blue) and upward (yellow) FACs at the ionospheric boundary of the simulation domain (the altitude of 110 km) obtained from three-dimensional MHD simulations with the ratio between the Hall and Pedersen conductance, $\Sigma_H/\Sigma_P = 0$ (a) and 2 (b). The input poleward electric field in the ionosphere between L-shells 3.2 and 3.4 is shown on the right. The color bars show the FAC density in μA/m^2.

Therefore, similar to a rayed auroral arc, a rayed structure resembling the observed Picket Fence is created by the IFI with the Σ_H/Σ_P ratio close to that in the SAID-I region.

Final remarks are in order. The feedback-unstable process involved in the Picket Fence creation is consistent with the MacDonald et al. (2018) observation that "over a several-minute period, unstable green features resembling a picket fence were observed propagating west. Up to six localized structures at a time were observed, typically for only one or two frames (of 4 s per frame). Their appearance suggests an unstable, turbulent, instability driven locally in the ionosphere." Further, as shows Figure S2 (Jia & Streltsov, 2014, Fig.7), the resulting structure depends on the actual value of Σ_H/Σ_P. That is, at smaller values the "pickets" turn at some angle relative to the $[E_X \times B_0]$ direction, like diagonal structures in some of the events.

3. On the STEVE Spectrum

The 630.0-nm, red-line emission of SAR arcs from the atomic oxygen 1-D state (O1D) is typically enhanced over the background by hundreds or even thousands of Rayleigh (e.g.,Mendillo & Wroten, 2019). In STEVE, the total luminosity of the red, green (from the O1S state), and blue (the second positive state of nitrogen, 2PN2) lines was enhanced by only ~160 Rayleigh (R), whereas a 400- to 800-nm continuum by 6200 R (Gillies et al., 2019, Table 1). SAR arcs are found inside plasma density troughs of $n_e \sim 3 \times 10^4$ cm^{-3} and $T_e \sim (3 \div 5) \times 10^3$ K related to subauroral polarization streams (SAPS) with flow speeds $v_d \sim 0.5$–1 km/s (e.g., Foster et al., 1994; Förster et al., 1999; Baumgardner et al., 2007). The STEVE-related SAID channels (MacDonald et al., 2018; Nishimura et al., 2019; Archer et al., 2019) have higher T_e up to $\sim 10^4$ K, larger speeds, $v_d \sim 4$–6 km/s, and deeper troughs, $n_e < 10^4$ cm^{-3}.

Gillies et al. (2019) discussed several reactions common for nightglow and raised a challenging question on the mechanism of the energy and momentum transfer to neutrals in a timely fashion to produce the observed STEVE continuum. Furthermore, calculating the O1D thermal excitation rate (e.g., Mantas & Carlson, 1991) with the above n_e and T_e values, we obtain the red-line intensity in STEVE/SAID comparable to, or even exceeding, that of SAR arcs (see Figure S3). Thus, another compelling question arises as to what inhibits thermal excitation in the STEVE region. In order to address these questions, we consider the impact of enhanced plasma flows and elevated temperature on the F-region ionosphere in more detail.

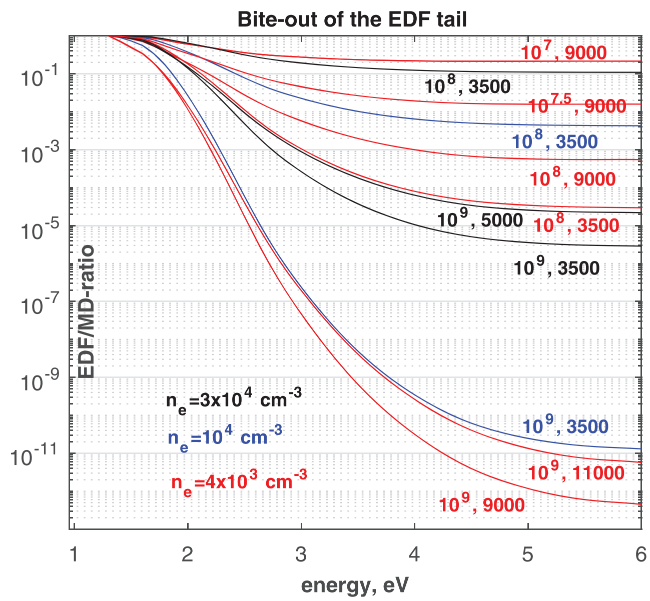

Figure 4. Variation of the ratio between the calculated electron distribution function (EDF) and a Maxwellian distribution (MD) with energy. The EDF was calculated with Mishin et al.'s (2000) solution for $n_e = 4 \times 10^3$ (red color), 10^4 (blue), and 3×10^4 (black) cm^{-3}, and the nitrogen density 10^7, 10^8, and 10^9 cm^{-3} with the electron temperature 3500, 5000, and 9000 K, as indicated.

First, we note that at $n_e < 10^{-3}[N_2]$, as typical for the SAID-related trough, the maximum rate of resonant excitation of N_2 vibrational states exceeds that of electron-electron collisions (e.g., Mishin et al., 2000). Hereinafter, $[X]$ stands for the density of neutral species X. In this case, the electron distribution function (EDF) has to be found from the kinetic equation accounting for vibrational excitation. Figure 4 shows the ratio between EDF and a Maxwellian distribution. Here EDF is calculated using Mishin et al.'s (2000) solution with plasma densities in SAID-related troughs, $n_e = 4 \times 10^3$ and 10^4 cm^{-3}, and SAR arcs, 3×10^4 cm^{-3}, with $[N_2] = 10^7$, $10^{7.5}$, 10^8, and 10^9 cm^{-3} and $T_e = 3500$, 5000, 9000, and 11000 K. The $[N_2]$ values are typical for altitudes, respectively, 400, 350, 300, and 240 km (e.g., Picone et al., 2002).

Evidently, for $n_e < 10^4$ cm^{-3} inelastic losses take a substantial "bite out" of the tail population at energies exceeding the O1D excitation threshold ≈1.96 eV, thereby practically shutting down thermal excitation below ~350 km ($[N_2] > 10^{7.5}$ cm^{-3}). The rate of dissociative recombination of O_2^+ is also small at low n_e and high T_e. Thus, the remaining viable source of excitation in STEVE is the suprathermal population, such as shown in Figure 3 (green and black). Notably, the flux of >50–10^3 eV electrons is greater than the photoelectron flux from the sunlit conjugate hemisphere in summer (e.g., Richards & Peterson, 2008, Fig. 5-6) by 3-5 times. Because photoelectrons yield tens of Rayleigh of ambient nightglow at 630.0 nm (e.g., Silverman, 1970), the suprathermal electrons appear to be sufficient to make the STEVE red-line emission of ~100 R (cf. Gillies et al., 2019, Fig. 1).

Furthermore, enhanced ion-neutral frictional (ohmic) heating in the F region leads to upwelling in the atmosphere. With the SAID/STEVE parameters, the enrichment of the STEVE region by molecular components is anticipated to be significant. Indeed, Millward et al. (1993) have numerically shown that ion-neutral frictional (ohmic) heating in the F region by a 0.2 V/m electric field (v_d ~4 km/s) increases the neutral density at altitudes ~400 km by a factor of 3 in about 10 min. Their results agree well with fast upwelling caused by a substorm-related ion drift surge ~5 km/s observed by a tristatic Fabry-Perot interferometer system and the EISCAT UHF radar near an altitude of 240 km (Aruliah et al., 2005). Similarly, about half an hour after the major storm onset, the CHAMP satellite detected almost doubled mass density at altitude ~400 km in the region of $v_d \geq 3$ km/s and $T_e \sim 6000$ K (Mishin et al., 2007).

The obvious corollary to the above is that the critical "bite-out" altitude rises by about one atmosphere scale height (~50 km). Note that strong plasma outflows in the STEVE events are indicated by upward ion speeds ~1 km/s (Nishimura et al., 2019, Fig. 2-3). As ohmic heating is proportional to v_d^2, atmosphere's upwelling is less efficient in SAR arcs usually associated with low-speed SAPS. Furthermore, as follows from Figure 4 (black curves), the EDF in SAR arcs is close to Maxwellian distribution at altitudes above ~250 km, and thermal excitation remains effective. Therefore, we conclude that the effect of vibrational excitation upon the thermal electron distribution determines the difference between the STEVE and SAR arc red-line brightness.

Gillies et al. (2019) discussed the chemiluminescent and radiative attachment reactions

$$\begin{aligned} NO + O \rightarrow NO_2^{\#} \xrightarrow{k_\lambda} NO_2 + h\nu \qquad (a) \\ O + e \rightarrow O^- + h\nu \qquad (b) \end{aligned} \tag{1}$$

as plausible sources of the STEVE continuum. Both, however, have the short-wavelength limit. Namely, the absolute rate constant, k_λ, in equation (1a) has a distinct maximum near $\lambda \approx$ 600 nm and drops to zero at ≈400 nm (Sutoh et al., 1980, Fig. 6). In turn, the frequency, ν, in equation (1b) is determined by the energy conservation, $h\nu = \varepsilon + \varepsilon_{aff}$, where ε is the electron energy and ε_{aff} = 1.456 eV is the affinity energy (e.g., Eletsky & Smirnov, 1983). For example, 1-eV electrons produce a ≈500-nm emission with the intensity determined by the number of these electrons. Thus, for $T_e \leq$ 11605 K or the mean energy of thermal electrons $\varepsilon \leq$ 1 eV, the intensity rapidly decreases at $\lambda <$ 500 nm.

Dzyubenko et al. (1986) invoked an endothermic reaction with the threshold ≈0.3 eV

$$N(^2D) + O_2 \rightarrow NO_2(^2\Sigma_u^+) \rightarrow NO_2(^2B_2) + h\nu \tag{2}$$

to interpret a 570- to 750-nm continuum observed in artificial aurora below 115 km. Indeed, dissociative recombination of NO^+ produces $N(^2D)$ atoms of the required energy (e.g., Torr & Torr, 1979). Their transition to the ground level, $N(^4S)$, yields a spectral peak from 516 to 521 nm (e.g., Chou et al., 2019), which is notable in the continuum (Gillies et al., 2019, Fig. 1). However, transition from the $^2\Sigma_u^+$ ground state to $^2B_2$ gives the short-scale limit ~570 nm.

Therefore, it seems unlikely that reactions (1) and (2) can explain the short-wavelength part of the spectrum, which is nearly flat between 400 and 800 nm (Gillies et al., 2019, Fig. 1).

4. Discussion and Conclusion

Let us first discuss the origin of energetic electrons inside the subauroral geospace (Nishimura et al., 2019, Figs. 2, 4). Such electrons are not anything unknown (e.g., Burke et al., 1995; Pedersen et al., 2007). They originate from early substorm injections and remain trapped during the substorm/storm recovery (Burke et al., 1995; Liemohn et al., 1998). Their presence with two SAID channels can be understood using the observation that the inner boundary of the substorm plasma sheet is controlled by the plasmapause (e.g., Mishin, 2013), while the plasmapause is controlled by the cross-tail, E_C, and SAID/SAPS electric fields (Goldstein et al., 2003). Figuratively, the plasmapause acts as a magnetosphere "power plant" (Streltsov & Mishin, 2018b) converting the kinetic energy of earthbound-ejected mesoscale plasma flows (MPFs) into the SAID electric field as follows.

Low ram pressure MPFs propagate from the reconnection site by virtue of the polarization electric field at the forefront (Mishin & Puhl-Quinn, 2007; Mishin, 2013), such as documented in laboratory experiments (e.g., Brenning et al., 2005). Eventually, the dense cold plasma at the plasmapause shorts out the polarization charge, so that the MPF's electrons stop and form the substorm plasma sheet/auroral boundary. The MPF's ions move further inward until the emerging SAID electric field stops them. As this process is inherently unstable, the turbulent plasmasphere boundary layer is formed, with the SAID channel as an integral part (see Figure S1). Once created, SAID may last in the subauroral region for a few hours (e.g., Anderson et al., 2001). In the case of several substorm breakups, the plasmapause moves inward between injections due to increasing E_C and plasmasphere erosion (Goldstein et al., 2003). Thus, the subsequent substorm MPF will form a new auroral boundary and SAID near the "fresh" plasmapause closer to the Earth. During the substorm recovery, the plasmapause moves outward leaving the remaining energetic electrons inside the plasmasphere with two SAID channels (see Figure S4).

SAID/SAPS-related density troughs are formed due to enhanced rates, $k_{1,2}$, of charge exchange of O^+ ions with N_2 (k_1) and O_2 (k_2) and subsequent fast recombination of NO^+ and O_2^+ ions (e.g., Schunk et al., 1976; Pavlov, 1996; Moffett et al., 1998) and ion outflows (Anderson et al., 1991). The depletion time is about $\tau \sim \left(k_1 \cdot [N_2] + k_2 \cdot [O_2]\right)^{-1} \sim$ 10–15 min. Once the density is depleted and the EDF tail is cut off (Figure 4), the thermal excitation of the red line is inhibited. This conclusion is true also for the F-region extent of the Picket Fence, which lacks of the red color, whereas the color in a rayed aurora gradually changes with altitude from green to red (Vallance Jones, 1974).

As noted Gillies et al. (2019) and show the above estimates regarding the STEVE continuum, its mechanisms are more puzzling, at least for the short-wavelength part. Taking account of vibrational and electronical states of participating molecular species may resolve the problem. In particular, Chou et al. (2019) specified transitions $N_2(C^3\Pi_u \rightarrow B^3\Pi_g)$ and $N_2(A^3\Sigma_u^+ \rightarrow X'\Sigma_g^+)$ in the ground states yielding emission lines at 391, 418, 420, 450, 485, 526, and 574 nm, that is, in the short-wavelength part. In general, transitions between vibrationally excited states produce around the lines multiple peaks corresponding to various combinations between vibrational energies (e.g., Vallance Jones, 1974; Piper, 1992). This is consistent with the Gillies et al. (2019, Fig. 1) spectrum.

It is known that vibrationally and electronically excited molecules play an important role in charge exchange and production of nitric oxide in high-temperature SAID and SAR arcs (e.g., Schunk et al., 1976; Pavlov, 1996; Moffett et al., 1998; Mishin et al., 2004) and auroral plasma (e.g., Mishin and Telegin, 1989; Campbell et al., 2006; 2007), respectively. More careful studies, both experimental and theoretical/numerical, are needed in order to characterize their effect on the emission spectrum in STEVE.

In conclusion, STEVE and the Picket Fence visualize processes occurring in the subauroral geospace during substorms. The Picket Fence structure is formed by feedback-unstable, SAID-driven magnetosphere-ionosphere interactions when the Hall conductance created by precipitating energetic electrons exceeds the Pedersen conductance. The bite out of the tail of the thermal electron distribution due to vibrational excitation of nitrogen molecules inhibits thermal excitation in STEVE. Thus, suprathermal electrons coming from the turbulent plasmasphere boundary layer appear to be the major excitation source. Because the chemiluminescent and radiative attachment reactions do not explain the short-wavelength part of the STEVE continuum, it is suggested that transitions between vibrationally excited molecular states in the SAID channel should be taken into account. The increased abundance of molecular components relative to atomic oxygen is related to atmosphere's upwelling due to enhanced ion-neutral drag and elevated temperature in the SAID region.

5. Data Availability Statement

FORTRAN and executable codes for 3-D simulations of FACs interacting with the ionosphere, data files to run simulations illustrated in Figure 2, and output files with 3-D distributions of FACs shown in Figure 2 are available as MISHIN-GRL-2019.zip archive from the Figshare.com/DOI:10.6084/m9.figshare.9856955

Acknowledgments
This work has been supported by the Air Force Office of Scientific ResearchLRIR 19RVCOR038 and Grant FA9550-19-1-0052. We thank B. Tulegenov for help with simulations and Y. Nishimura for THEMIS-E data. The THEMIS and DMSP data are available through http://themis.ssl.berkeley.edu and http://cedar.openmadrigal.org websites.

References

Anderson, P., Carpenter, D., Tsuruda, K., Mukai, T., & Rich, F. (2001). Multisatellite observations of rapid subauroral ion drifts (SAID). *Journal of Geophysical Research*, *106*(A12), 29585–29599.

Anderson, P., Heelis, R., & Hanson, W. (1991). The ionospheric signatures of rapid subauroral ion drifts. *Journal of Geophysical Research*, *96*, 5785.

Archer, W., Gallardo-Lacourt, B., Perry, G., St.-Maurice, J.-P., Buchert, S., & Donovan, E. (2019). Steve: The optical signature of intense subauroral ion drifts. *Geophysical Research Letters*. https://doi.org/10.1029/2019GL082687

Archer, W., St.-Maurice, J.-P., Gallardo-Lacourt, B., Perry, G., Cully, C., Donovan, E., et al. (2019). The vertical distribution of the optical emissions of a Steve and Picket Fence event. *Geophysical Research Letters*, *46*. https://doi.org/10.1029/2019GL084473

Aruliah, A., Griffin, E., Aylward, A., Ford, E., Kosch, M., Davis, C., et al. (2005). First direct evidence of meso-scale variability on ion-neutral dynamics using co-located tristatic FPIs and EISCAT radar in Northern Scandinavia. *Annales de Geophysique*, *23*, 147–162.

Baumgardner, J., Wroten, J., Semeter, J., Kozyra, J., Buonsanto, M., Erickson, P., & Mendillo, M. (2007). A very bright SAR arc: Implications for extreme magnetosphere-ionosphere coupling. *Annales de Geophysique*, *25*, 2593–2608.

Brenning, N., Hurtig, T., & Raadu, M. (2005). Conditions for plasmoid penetration across abrupt magnetic barriers. *Physics of Plasmas*, *12*, 012309.

Burke, W., Rubin, A., Hardy, D., & Holeman, E. (1995). Banded electron structures in the plasmasphere. *Journal of Geophysical Research*, *100*, 7759–7769.

Campbell, L., Cartwright, D., & Brunger, M. (2007). Role of excited N_2 in the production of nitric oxide. *Journal of Geophysical Research*, *112*, A08303. https://doi.org/10.1029/2007JA012337

Campbell, L., Cartwright, D., Brunger, M., & Teubner, P. (2006). Role of electronic excited N_2 in vibrational excitation of the N_2 ground state at high latitudes. *Journal of Geophysical Research*, *111*, A09317. https://doi.org/10.1029/2005JA011292

Chou, S.-L., Lo, J.-I., Peng, Y.-C., Lu, H.-C., Cheng, B.-M., & Ogilvie, J. (2019). Emission spectra of atomic and molecular nitrogen from photolysis of ammonia in solid neon. *AIP Advances*, *9*, 055311. https://doi.org/10.1063/1.5096280

Dzyubenko, N., Ivchenko, V., Milinevsky, G., Mishin, E., & Telegin, V. (1986). The "continuum" in the radiation of an artificial polar aurora. *Geomagn. and Aeronomy, English Transl.*, *23*, 429–430.

Eletsky, A., & Smirnov, B. (1983). Elementary nonradiative processes. In A. Galeev, & R. Sudan (Eds.), *Basic plasma physics*, (Vol. 1, pp. 49–70). Amsterdam: North-Holland.

Förster, M., Foster, J., Smilauer, J., Kudela, K., & Mikhailov, A. (1999). Simultaneous measurements from the Millstone H ill radar and the Active satellite during the SAID/SAR arc event of the March 1990 CEDAR storm. *Annales de Geophysique*, *17*, 389–404.

Foster, J., Buonsanto, M., Mendillo, M., Notingham, D., Rich, F., & Denig, W. (1994). Coordinated stable auroral red arc observations: Relationship to plasma convection. *Journal of Geophysical Research*, *99*, 11,429–11,439.

Gallardo-Lacourt, B., Liang, J., Nishimura, Y., & Donovan, E. (2018). On the origin of STEVE: Particle precipitation or ionospheric skyglow? *Geophysical Research Letters*, *45*, 7968–7973.

Gallardo-Lacourt, B., Nishimura, Y., Donovan, E., Gillies, D., Perry, G., Archer, W., et al. (2018). A statistical analysis of STEVE. *Journal of Geophysical Research: Space Physics*, *123*, 9893–9905. https://doi.org/10.1029/2018JA025368

Gillies, D., Donovan, E., Hampton, D., Liang, J., Connors, M., Nishimura, Y., et al. (2019). First observations from the TREx spectrograph: The optical spectrum of STEVE and the Picket Fence phenomena. *Geophysical Research Letters*, *46*, 7207–7213. https://doi.org/10.1029/2019GL083272

Goldstein, J., Sandel, B., Hairston, M., & Reiff, P. (2003). Control of plasmaspheric dynamics by both convection and subauroral polarization stream. *Geophysical Research Letters*, *30*, 2243–2246.

Jia, N., & Streltsov, A. (2014). Ionospheric feedback instability and active discrete auroral forms. *Journal of Geophysical Research: Space Physics*, *119*, 2243–2254.

Liemohn, M., Khazanov, G., & Kozyra, J. (1998). Banded electron structure formation in the inner magnetosphere. *Geophysical Research Letters*, *25*, 877–880.

MacDonald, E., Donovan, E., Nishimura, Y., Case, N., Gillies, D. M., Gallardo-Lacourt, B., et al. (2018). New science in plain sight: Citizen scientists lead to the discovery of optical structure in the upper atmosphere. *Science Advances*, *4*(3), eaaq0030.

Mantas, G., & Carlson, H. (1991). Reexamination of of the O(^{3}P→ ^{1}D) excitation rate by thermal electron impact. *Geophysical Research Letters*, *18*, 159–162.

Mendillo, M., & Wroten, J. (2019). Modeling stable auroral red (SAR) arcs at geomagnetic conjugate points: Implications for hemispheric asymmetries in heat fluxes. *Journal of Geophysical Research: Space Physics*, *124*, 6330–6342. https://doi.org/10.1029/2019JA026904

Millward, G., Quegan, S., Moffett, R., Fuller-Rowell, T., & Rees, D. (1993). A modelling study of the coupled ionospheric-thermospheric response to an enhanced high-latitude electric field event. *Planetary and Space Science*, *41*, 45–56.

Mishin, E. (2013). Interaction of substorm injections with the subauroral geospace: 1. Multispacecraft observations of SAID. *Journal of Geophysical Research: Space Physics*, *118*, 5782–5796.

Mishin, E., Burke, W., & Viggiano, A. (2004). Stormtime subauroral density troughs: Ion-molecule kinetic effects. *Journal of Geophysical Research*, *109*, A10301.

Mishin, E., Carlson, H., & Hagfors, T. (2000). On the electron distribution function in the F region and airglow enhancements during HF modification experiments. *Geophysical Research Letters*, *27*, 2857–2860.

Mishin, E., Marcos, F., Burke, W., Cooke, D., Roth, C., & Petrov, V. (2007). Prompt thermospheric response to the 6 November 2001 magnetic storm. *Journal of Geophysical Research*, *112*, A05313.

Mishin, E., Nishimura, Y., & Foster, J. (2017). SAPS/SAID revisited: A causal relation to the substorm current wedge. *Journal of Geophysical Research, Space Physics*, *122*, 8516–8535. https://doi.org/10.1002/2017JA024263

Mishin, E., & Puhl-Quinn, P. (2007). SAID: Plasmaspheric short circuit of substorm injections. *Geophysical Research Letters*, *34*, L24101.

Mishin, E., & Sotnikov, V. (2017). The turbulent plasmasphere boundary layer and the outer radiation belt boundary. *Plasma Physics and Controlled Fusion*, *59*, 124003.

Mishin, E., & Telegin, V. (1989). Effects of plasma turbulence in aurora. *Geomagn.and Aeronomy., Engl Edition*, *29*, 1–13.

Moffett, R., Ennis, A., Bailey, G., Heelis, R., & Brace, L. (1998). Electron temperatures during rapid subauroral ion drift events. *Annales de Geophysique*, *16*, 450.

Nishimura, Y., Gallardo-Lacourt, B., Zou, Y., Mishin, E., Knudsen, D., Donovan, E., et al. (2019). Magnetospheric signatures of STEVE: Implication for the magnetospheric energy source and inter-hemispheric conjugacy. *Geophysical Research Letters*, *46*, 5637–5644. https://doi.org/10.1029/2019GL082460

Pavlov, A. (1996). Mechanisms of the electron density depletion in the SAR arc region. *Annales de Geophysique*, *14*, 211–221.

Pedersen, T., Mishin, E., & Oksavik, K. (2007). Observations of structured optical emissions and particle precipitation equatorward of the traditional auroral oval. *Journal of Geophysical Research*, *112*, A10208.

Picone, J., Hedin, A., Drob, D., & Aikin, A. (2002). NRLMSISE-00 empirical model of the atmosphere: Statistical comparisons and scientific issues. *Journal of Geophysical Research*, *107*, 1468.

Piper, L. (1992). Energy transfer studies on N_2(X,V) and N_2(B). *The Journal of Chemical Physics*, *97*, 270–275.

Puhl-Quinn, P., Matsui, H., Mishin, E., Mouikis, C., Kistler, L., Khotyaintsev, Y., et al. (2007). Cluster and DMSP observations of SAID electric fields. *Journal of Geophysical Research*, *112*, A05219.

Richards, P., & Peterson, W. (2008). Measured and modeled backscatter of ionospheric photoelectron fluxes. *Journal of Geophysical Research*, *113*, A08321. https://doi.org/10.1029/2008JA013092

Robinson, R. M., Vondrak, R. R., Miller, K., Dabbs, T., & Hardy, D. (1987). On calculating ionospheric conductances from the flux and energy of precipitating electrons. *Journal of Geophysical Research*, *92*, 2565–2569.

Schunk, R., Banks, P., & Raitt, W. (1976). Effect of electric fields and other processes upon the nighttime high-latitude F layer. *Journal of Geophysical Research*, *81*, 3271.

Silverman, S. (1970). Night airglow phenomenology. *Space Science Reviews*, *11*, 341–379.

Streltsov, A., & Foster, J. (2004). Electrodynamics of the magnetosphere-ionosphere coupling in the nightside subauroral zone. *Physics of Plasmas*, *11*, 1260–1267.

Streltsov, A., & Mishin, E. (2003). Numerical modeling of localized electromagnetic waves in the nightside SubAuroral zone. *Journal of Geophysical Research*, *108*, 1332.

Streltsov, A., & Mishin, E. (2018a). On the existence of ionospheric feedback instability in the Earth's magnetosphere-ionosphere system. *Journal of Geophysical Research: Space Physics*, *123*, 8951–8957.

Streltsov, A., & Mishin, E. (2018b). Ultralow frequency electrodynamics of magnetosphere-ionosphere interactions near the plasmapause during substorms. *Journal of Geophysical Research, Space Physics*, *123*, 7441–7451.

Sutoh, M., Morioka, Y., & Nakamura, M. (1980). Absolute rate constant for the chemiluminescent reaction of atomic oxygen with nitric oxide. *The Journal of Chemical Physics*, *72*, 20–24. https://doi.org/10.1063/1.438878

Torr, D., & Torr, M. (1979). Chemistry of the thermosphere and ionosphere. *Journal of Atmospheric and Terrestrial Physics*, *41*, 797–839. https://doi.org/10.1016/0021-9169(79)90126-0

10.1029/2019GL085446

Trakhtengertz, V., & Feldstein, A. (1991). Turbulent Alfvén boundary layer in the polar ionosphere. 1. Excitation conditions and energetics. *Journal of Geophysical Research*, *96*, 19363–19374.
Vallance Jones, A. (1974). *Aurora. Geophys & Astrophys. Monographs*, (Vol. 9, p. 301). Boston: D. Reidel.